

# Automated Image Analysis Methods for 3-D Quantification of the Neurovascular Unit From Multichannel Confocal Microscope Images

Gang Lin,<sup>1</sup> Chris S. Bjornsson,<sup>2</sup> Karen L. Smith,<sup>2</sup> Muhammad-Amri Abdul-Karim,<sup>1</sup> James N. Turner,<sup>2</sup> William Shain,<sup>2</sup> and Badrinath Roysam<sup>1\*</sup>

<sup>1</sup>Department of Electrical, Computer, and Systems Engineering, Rensselaer Polytechnic Institute, Troy, New York

<sup>2</sup>Laboratory of Nervous System Disorders, New York State Department of Health, Wadsworth Center, Albany, New York

Received 14 December 2004; Revision 9 March 2005; Accepted 11 March 2005

**Background:** There is a need for integrative and quantitative methods to investigate the structural and functional relations among elements of complex systems, such as the neurovascular unit (NVU), that involve multiple cell types, microvasculatures, and various genomic/proteomic/ionic functional entities.

**Methods:** Vascular casting and selective labeling enabled simultaneous three-dimensional imaging of the microvasculature, cell nuclei, and cytoplasmic stains. Multidimensional segmentation was achieved by (i) bleed-through removal and attenuation correction; (ii) independent segmentation and morphometry for each corrected channel; and (iii) spatially associative feature computation across channels. The combined measurements enabled cell classification based on nuclear morphometry, cytoplasmic signals, and distance from vascular elements. Specific spatial relations among the NVU elements could be quantified.

**Results:** A software system combining nuclear and vessel segmentation codes and associative features was con-

structed and validated. Biological variability contributed to misidentified nuclei (9.3%), undersegmentation of nuclei (3.7%), hypersegmentation of nuclei (14%), and missed nuclei (4.7%). Microvessel segmentation errors occurred rarely, mainly due to nonuniform lumen staining.

**Conclusions:** Associative features across fluorescence channels, in combination with standard features, enable integrative structural and functional analysis of the NVU. By labeling additional structural and functional entities, this method can be scaled up to larger-scale systems biology studies that integrate spatial and molecular information. © 2005 Wiley-Liss, Inc.

**Key terms:** multidimensional image analysis; three-dimensional blob segmentation; three-dimensional microvessel tracing; object features; interobject features; confocal microscopy; vascular casting; neurovascular unit

The structural and functional complexities of the nervous system are monumental. At the cellular level, neurons and supporting glia are intimately linked to the neurovasculature that supports them: increased neuronal activity places greater demands on the circulatory system and increases local cerebral blood flow by regulating vascular tone (functional hyperemia) (1,2). The neurovasculature can also influence neuronal function, especially in response to injury through coordinated release of neuroangiogenic factors (1,3,4). Astrocytes mediate many of these interactions (2,5). In many cortical regions the vascular architecture recapitulates the underlying neural organization (6,7). The organization and interplay among neurons, glia, and blood vessels have fostered the concept of the neurovascular unit (NVU) as a distinctive structural and functional entity within the central nervous system that is worthy of study in its own right (1,3,8).

A quantitative structural elucidation of NVU necessarily requires three-dimensional (3-D) imaging to describe the

structures of the individual NVU elements and their relative spatial juxtaposition and organization. A complete functional elucidation of the NVU requires some form of molecular imaging to map the presence and spatial distribution of various functional genomic and proteomic markers. All of this must be done with subcellular resolution. These considerations motivate the use of modern optical microscopy as the investigative tool of choice.

Contemporary techniques allow selective fluorescent labeling of multiple structural and functional entities

Contract grant sponsor: NSF Engineering Research Centers Program; Contract grant number: EEC-9986821; Contract grant sponsor: National Institutes of Health; Contract grant numbers: AG18230, AG023309 NIBIB R01-EB000359, NINDS R01-NS1044287.

G. Lin and C. S. Bjornsson contributed equally to this work.

\*Correspondence to: Prof. B. Roysam, JEC 7010, Rensselaer Polytechnic Institute, Troy, NY 12180-3590.

E-mail: roysam@ecse.rpi.edu

Published online 2 June 2005 in Wiley InterScience (www.interscience.wiley.com).

DOI: 10.1002/cyto.a.20149

within the NVU. This, when combined with multispectral confocal/multiphoton microscopy provides the opportunity to generate detailed and extensive 3-D imagery of these entities in a manner that preserves their anatomic characteristics and important spatial relations among them. Thick tissue samples containing multiple labeled cell types can be used to study how the organization of the NVU varies between cortical layers and brain regions and to investigate NVU changes associated with disease and injury. From a systems biology perspective (9), modern microscopy is valuable for its ability to record structures and functional markers in intact tissue and avoid the need to fragment cells through preparation of thin tissue sections. Spatial distributions and interactions among multiple structural and functional markers in intact tissue are preserved unlike biochemical assays, gene arrays (10), and flow cytometry (11), in which spatial information is inevitably disrupted. Although these methods do provide temporal data, they do not relate it with spatial information. On a practical basis, imaging is also attractive for its intuitive visual confirmation capability. Overall, image-based approaches to investigating the NVU offer key advantages and a complement to other strategies.

Recently, there has been an explosive growth in the sophistication of optical microscopy (12–15). Multispectral imaging, with its ability to disentangle overlapping fluorescent emissions, enables simultaneous observation of multiple labels, providing a wealth of molecular data (16–18). Burgeoning fluorophore libraries now permit ever larger numbers of highly specific structural and functional entities (genomic, proteomic, and ionic, among others) to be labeled simultaneously (18,19). With the widespread availability of axially resolved imaging techniques, notably confocal and multiphoton microscopy, 3-D imaging is now routine. With the advent of technologies for handling time-resolved, 3-D imaging of live specimens, there is reason to be optimistic about the future of optical microscopy in elucidating the NVU. In the future, such analyses can also be expected to be possible on a large scale using seamless large-field high-resolution imaging by automatic montaging (20–23). In this paper, we use the term *multidimensional microscopy* to refer to the combination of spatial, temporal, and spectral dimensions accessible by modern microscopy.

Although multidimensional imaging as noted above can provide a wealth of detailed and sophisticated data, it has remained difficult to translate this massive data into quantitative insight. Automated image analysis is the computational process of making quantitative structural and functional measurements from an image in a manner that avoids/minimizes subjective errors. The past decade has resulted in significant progress in 3-D image analysis. For instance, rapid and automated segmentation of fluorescently labeled blob-like structures such as cell nuclei and quantitation of various genomic signals relative to this segmentation are now a mature and routinely used technology (24–26). Rapid, accurate, and robust 3-D tracing and morphometry of tube-like structures such as neuronal processes and microvasculature have matured separately to a

level that they can be employed routinely (27–31). At the very least, the automated methods described here can enable a major reduction in tedium and manual effort ordinarily associated with image analysis. At a higher level, they offer several advantages over manual analysis, including the handling of high-dimensional data, speed, consistency, quantitative accuracy, and the capability to query complex spatial databases.

The goal of this work is to demonstrate the practical feasibility of extending and integrating these prior advances in a manner that addresses the needs posed by complex systems such as the NVU. *The main idea is to identify and quantify the associations between spatial and functional entities revealed by various fluorophores in a manner that is insightful yet practically feasible.* Specifically, segmentations of objects such as cell nuclei and the microvasculature can be thought of as local structural references, or “spatial anchors,” relative to which a multitude of fluorescent markers can be readily associated and mapped. Further, with imaging, it becomes possible to link the molecule-specific information available from fluorescence microscopy with conventional image cytometric measurements such as nuclear size, shape, and texture to derive additional quantitative descriptions that cannot be generated by either approach individually. The end result of the analysis described here is a multidimensional tabular morphometric summary that can be stored in database form or spreadsheets for graphing, query, and further quantitative analysis. We provide illustrative examples of such analysis.

## MATERIALS AND METHODS

### Specimen Preparation and Imaging

Laser scanning confocal microscopy was used to collect 3-D images of triple-labeled brain tissue slices highlighting three key constituents of the NVU: the microvasculature, cell nuclei, and Nissl substance. The microvasculature was filled using a vascular casting protocol described below. A nucleic acid stain was used to label nuclei of all cells, including neurons, endothelial cells, astrocytes, microglia, oligodendrocytes, smooth muscle cells, and pericytes. Two possible approaches to distinguish among these cell types include (i) the use of a distinguishing cytoplasmic stain and (ii) the use of morphometric data for the nuclei, such as shape, texture, size, and spatial location relative to the microvasculature. We used Nissl staining to illustrate the former approach and describe how these two can be combined in the next section. The use of Nissl staining is just one example of the potential of this technique to highlight different elements of the NVU.

Male Sprague-Dawley rats (Taconic Farms, NY, USA) were housed at standard temperature in a light-controlled environment, with ad libitum access to food and water. All protocols were approved by the International Animal Care and Use Committee of the Wadsworth center. Animals weighing 100 to 130 g were anesthetized with tribromoethanol (23 mg/100 g body weight) and transcardially

perfused using a constant-pressure perfusion apparatus (32), which allowed us to record perfusion pressure and flow rate. Two hundred milliliters of heparinized (1 U/ml) isotonic buffer (200 ml) was perfused through the ascending aorta at 200 mmHg before fixation with 200 ml of 4% paraformaldehyde in phosphate buffer at 110 to 130 mmHg. The elevated buffer pressure was essential to achieve adequate fixation. We recorded flow rates for buffer between 110 and 130 ml/min and fixative flow rates between 50 and 75 ml/min. During fixation, a premixed solution consisting of 40 ml of Mercox-B (Ladd Research, Williston, VT, USA), 10 ml of methyl methacrylate (Fluka, St. Gallen, Switzerland), and 15 mg of rhodamine B (Sigma-Aldrich, St. Louis, MO, USA) was added to 0.8 ml of catalyst (Ladd Research) and poured into a 60-ml syringe casing to prepare the fluorescent casting resin (33). A rubber stopper fitted with ports connected to a rubber bulb and a sphygmomanometer was placed over the back of the syringe casing, and the spout was connected to the perfusion needle. Mercox was injected at 200 to 300 mmHg and left to polymerize for 30 min before brains were harvested. Mercox-injected brains were allowed to polymerize further at 37°C for 3 to 4 h in 4% paraformaldehyde before storage overnight at 4°C. After 24 h, the brain was washed in phosphate buffered saline. Slices approximately 1 mm thick were cut by hand with a fresh razor blade. Brain slices were permeabilized in 0.2% Triton X-100 in HEPES-buffered Hanks (HBHS) for 30 min, washed in HBHS, and stained overnight using CyQuant (1:1,000; Molecular Probes, Eugene, OR, USA) and NeuroTrace (1:125; Molecular Probes). Slices were then washed and mounted in HBHS.

Images were collected using a NORAN laser scanning confocal attachment and an Olympus IX-70 microscope fitted with a 40× W/1.15 NA objective. Images were 192 × 180 μm (0.375 μm/pixel). Z-series image stacks were collected using 1.0-μm steps. Photomultiplier gain and black level settings were optimized to achieve the optimal dynamic range for each 3-D image stack independently by using a “range check” pseudocolored map on the brightest optical section of the sample. Photomultiplier gain and black level settings were optimized for each image separately to achieve the optimal dynamic range. Figure 1 shows a maximum intensity projection display, along the axis orthogonal to the display planes, of a representative three-color 3-D confocal microscope image stack, as part of a screen view of the integrative software system. The cell nuclei (blobs) are displayed in green. Blood vessels (tubes) are displayed in red, and the unstructured cloud-like Nissl cytoplasmic stain is displayed in blue. Three distinctive blob morphologies can be observed in the data: larger, dimmer, and more heterogeneous neuronal nuclei; smaller, brighter and more uniform glia; and flat, intense endothelial cells. Differences in cloud shape and volume can also be used to distinguish larger pyramidal neurons from other neuron types. Figure 2 summarizes the main procedures for automated analysis of these 3-D image stacks containing different types of object. The detailed process of analyzing datasets such as this are described below.

## Image Preprocessing

The effects of common imaging artifacts include bleed-through of signals between imaging channels, intensity nonuniformity in  $x$ ,  $y$ , and  $z$ , and presence of uninteresting/confounding objects. The bleed-through elimination used in this work was based on simple subtraction. Sometimes, nonuniform illumination causes different parts of the image to exhibit different contrast or brightness. Alternatively, foreground objects may appear grainy. Figure 3 illustrates several imaging artifacts, which must be eliminated using a preprocessing step. First, signal attenuation correction is useful to rectify depth-dependent attenuation of signals (34–36). We simply linearly scale the voxel intensity of each slice along the depth of the image stack so that the average foreground intensity of all slices has the same value. Without segmentation, foreground region is defined as the voxels that have the intensity value greater than a specified threshold, which is calculated using the statistics of the image, i.e., intensity mean and variation. Then, median filtering with kernel size 5 (37,38) is used to remove the shot noise in the image. Morphologic operations in gray scale (39,40), i.e., morphologic close and open, are used in that order with a kernel size of  $7 \times 7 \times 3$  to remove noise and smooth out nonuniformities of foreground intensity, such as small island-like artifacts and holes inside objects.

Another rationale to preprocessing is to generate “standardized images” where one segmentation method is used for images coming from different sources. For example, images of a similar biological object from different experiments may exhibit different contrast and illumination characteristics, requiring them to be “standardized” before segmentation. At the other extreme, images of neuronal processes and vasculature may be preprocessed to accentuate the tube-like morphology of these biological objects (41).

Note that many of the neuronal nuclei are very distinct in our images, as shown in green in Figure 3. These cells possess large nuclei with prominent nucleoli and a clear ring of heterochromatin associated with the nuclear lamina. The euchromatin occupying most of the nuclear volume takes on very little stain, making these nuclei appear much dimmer than the surrounding glia and endothelial cells. In addition, cross-talk was observed between the Cy5 (Nissl) channel and the CyQuant (nuclei) channel around these neurons in some images. Therefore, the following special preprocessing steps were needed: the Cy5 (Nissl) channel was detected and then subtracted from the nuclei channel to eliminate bleed-through. The interior region of the rings around dim nuclei was masked out to be extracted using lower foreground threshold during the subsequent segmentation.

## Segmentation Methods

Segmentation is the process of identifying and delineating “objects” in the image data, which is the critical first step in our image analysis. The main objects of interest in



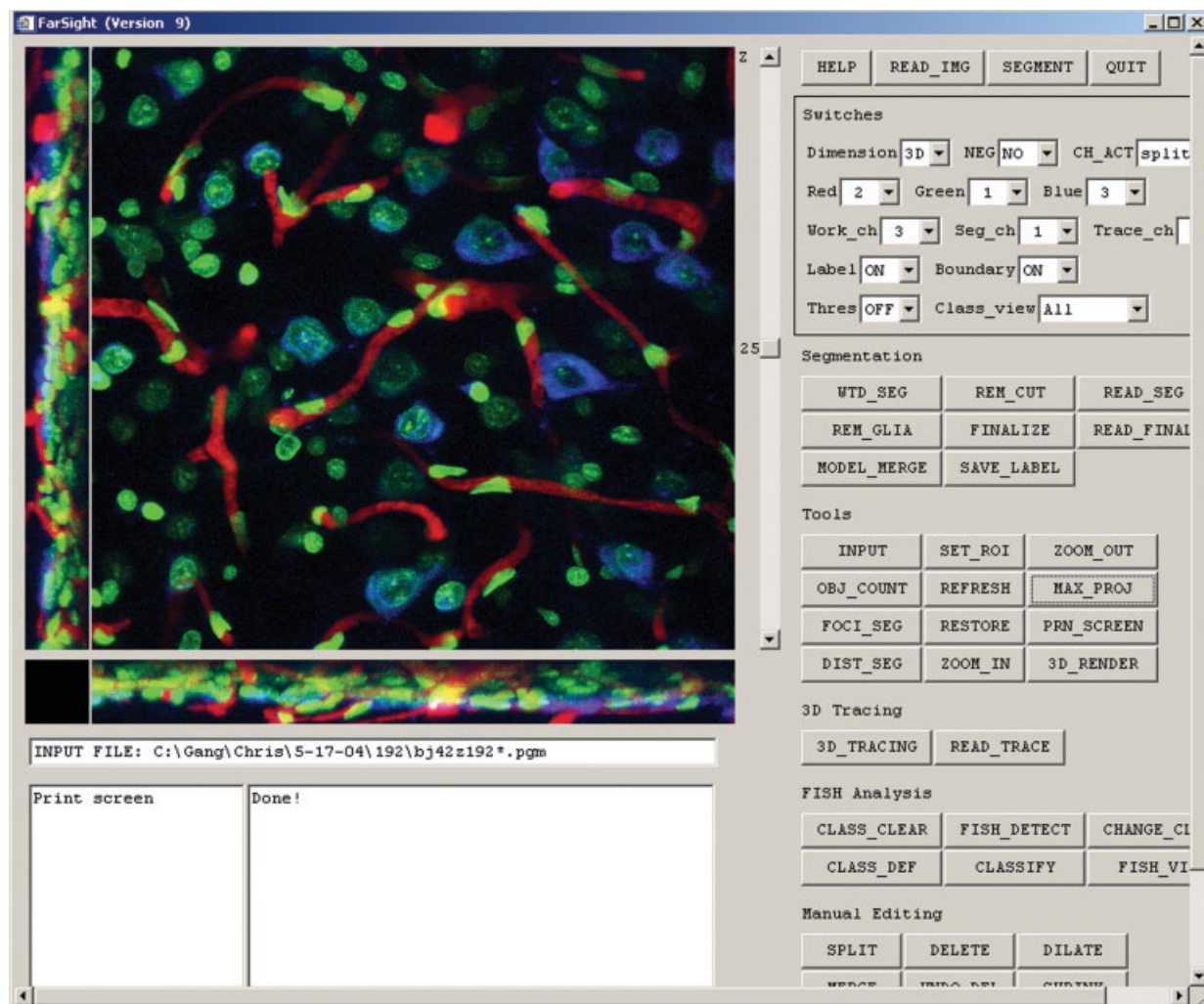


Fig. 1. A screen view of the integrative software system showing a sample triple-label dataset displayed as a set of three projections ( $x$ - $y$ ,  $y$ - $z$ , and  $x$ - $z$ ). Cell nuclei (blob-like objects) are shown in green. Blood vessels (tube-like objects) are shown in red, and the unstructured cloud-like object in the third channel (blue) is the Nissl cytoplasmic stain. Notice that three general blob morphologies can be distinguished: larger, dimmer, and more heterogenous neuronal nuclei; smaller, brighter and more uniform glia; and flat, intense endothelial cells. Differences in cloud shape and volume can also be used to distinguish larger pyramidal neurons from other neuron types.

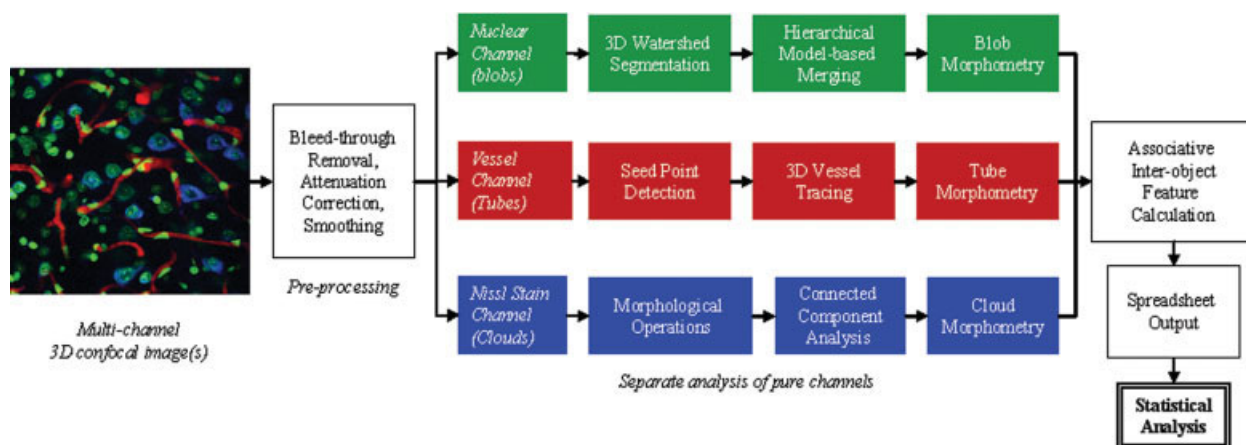


Fig. 2. Illustrating the main steps for automated analysis of multichannel 3-D confocal image stacks containing different object classes. The separate imaging of cytological objects in different channels enables a “divide and conquer” approach to the analysis of such complex systems. Only the main steps in the analysis of each pure channel are noted in this simplified diagram. The details are described in other cited papers.

the NVU include the microvasculature, the cell nuclei, and various genomic or proteomic markers. The microvasculature is representative of a broader class of image objects referred to in the image analysis literature as “tubes.” The cell nuclei are similarly representative of “blobs,” whereas the Nissl bodies appear as “clouds” (42). Another type of object that does not appear in our examples but is nevertheless relevant to the NVU is genomic/proteomic “foci” or punctate (25,43–46). The specimen preparation and imaging procedure outlined above provides a powerful form of simplification and extensibility: each of the fluorescent channels is “pure” in the sense that it contains only one type of object. This greatly simplifies the image analysis task.

An integrated and extensible software package, termed FARSIGHT (Fluorescence Association Rules for Quantitative Insight) was developed that combines several separately developed packages, especially blob segmentation and fluorescence in situ hybridization quantitation (25), and tube segmentation (30) under a common software platform provided by IDL (Interactive Data Language, Research Systems, Boulder, CO, USA). Figure 1 shows a screen view of this integrative software package.

**Nuclear channel segmentation.** The fluorescently labeled cell nuclei (green channel) in Figure 1 are examples of 3-D blobs, by far the most common type of object of interest in automated image analysis. These apparently simple objects nevertheless provide a rich set of challenges from the standpoint of automated image analysis (24).

The prior literature describes two main approaches to blob segmentation: top-down and bottom-up methods. Top-down segmentation is guided by some a priori knowledge of the morphology of objects in question, such as expected object volumes and shapes (47,48). Bottom-up approaches start with an oversegmentation of the image and iteratively merge regions based on some measure of similarity (49–53). Some methods operate iteratively by grouping together neighboring voxels that have similar features (54,55) and graph-based clustering (56–58) and splitting groups of voxels that are dissimilar, such as the widely used watershed algorithm (34,59–62).

As revealed in the green channel in Figure 1, tightly packed cell layers, which often result in the appearance of “touching objects” in the image stacks, present the main segmentation challenge. Lin et al. (24) described an improved algorithm using two ideas: (i) a distance transform combining intensity gradients and geometric distance for the watershed object separation step and (ii) deliberate initial oversegmentation, followed by statistical model-based merging. In Lin et al. (26), a more accurate, recursive, tree-based algorithm that can consider multiple object fragments simultaneously for the merging was introduced. The main ideas behind these methods are summarized below.

The watershed algorithm is widely used for efficient connected object separation (59–62). Its main limitations arise from the fact that it relies on touching objects exhibiting an often unreliable “neck” in the region of contact. Considerable effort has been devoted to the design of

algorithms for generating the correct set of “geometric markers” to guide the object segmentation. To overcome this challenge, image gradient can be used (63–65). Lin et al. (24) proposed a “gradient-weighted distance transform” that combines object separation hints derived from geometric and intensity cues in the image data. Specifically, the geometric-distance transform  $D$  (66), and the gradient transform  $G$  (24) are combined into a single representation that captures the object separation cues available in the data, as given by the following formula.

$$\mathbf{D}' = \mathbf{D} \times \exp\left(1 - \frac{\mathbf{G} - G_{\min}}{G_{\max} - G_{\min}}\right) \quad (1)$$

where  $G_{\min}$  and  $G_{\max}$  are the minimum and maximum values of the gradient  $G$  needed for normalization. This expresses the object separation cue that the voxels with larger gradient values tend to lie on the boundary of an object. In practice, the watershed algorithm requires the inverse of this distance transformation. This inverse is denoted  $\mathbf{T}$  and is computed as follows:

$$\mathbf{T} = S_g(\max[\mathbf{D}'] - \mathbf{D}'), \quad (2)$$

where  $\max(\mathbf{D}')$  is the global maximum within the distance images, and  $S_g$  represents a Gaussian smoothing operator (38) to overcome uneven cell staining. This combined transformation is effective in discriminating touching nuclear clusters even when they do not exhibit the characteristic bottleneck-shaped pattern.

To correct the still remnant oversegmentation after the above watershed segmentation, it is necessary to detect and break (eliminate) false watershed surfaces and thereby merge the objects (24,35). Currently, the best methods rely on a quantitative mathematical model of the objects of interest (i.e., the nuclei) that is described by a vector of features, denoted  $X_c$ , and includes the volume, texture, convexity, circularity and shape. The merging score based on these features assuming that they are Gaussian distributed is given by:

$$S_c = p(X_c) = \frac{1}{(2\pi)^{m/2} |\Sigma_x|^{1/2}} \exp\left(-\frac{1}{2} \sqrt{[X_c - \bar{X}]^T \Sigma_x^{-1} [X_c - \bar{X}]}\right) \quad (3)$$

where  $\bar{X}$  and  $\Sigma_x$  are the mean and covariance matrix of the training feature set, respectively, which are obtained from some example intact nuclei in the given image stack.

Intuitively, the merging decisions can be based on the following two criteria: (i) the merging score  $S_{c_w}$ , i.e., the score of the combined object by nuclei  $c_w^1$  and  $c_w^2$  and watershed surface  $w$ , should be higher than the score of either nucleus  $S_{c_w^1}^1$  or  $S_{c_w^2}^2$  before merging. (ii) The gradient of watershed surface  $w$  should be relatively large compared with the gradient of nuclei  $c_w^1$  and  $c_w^2$ . This is based on assuming that intra-

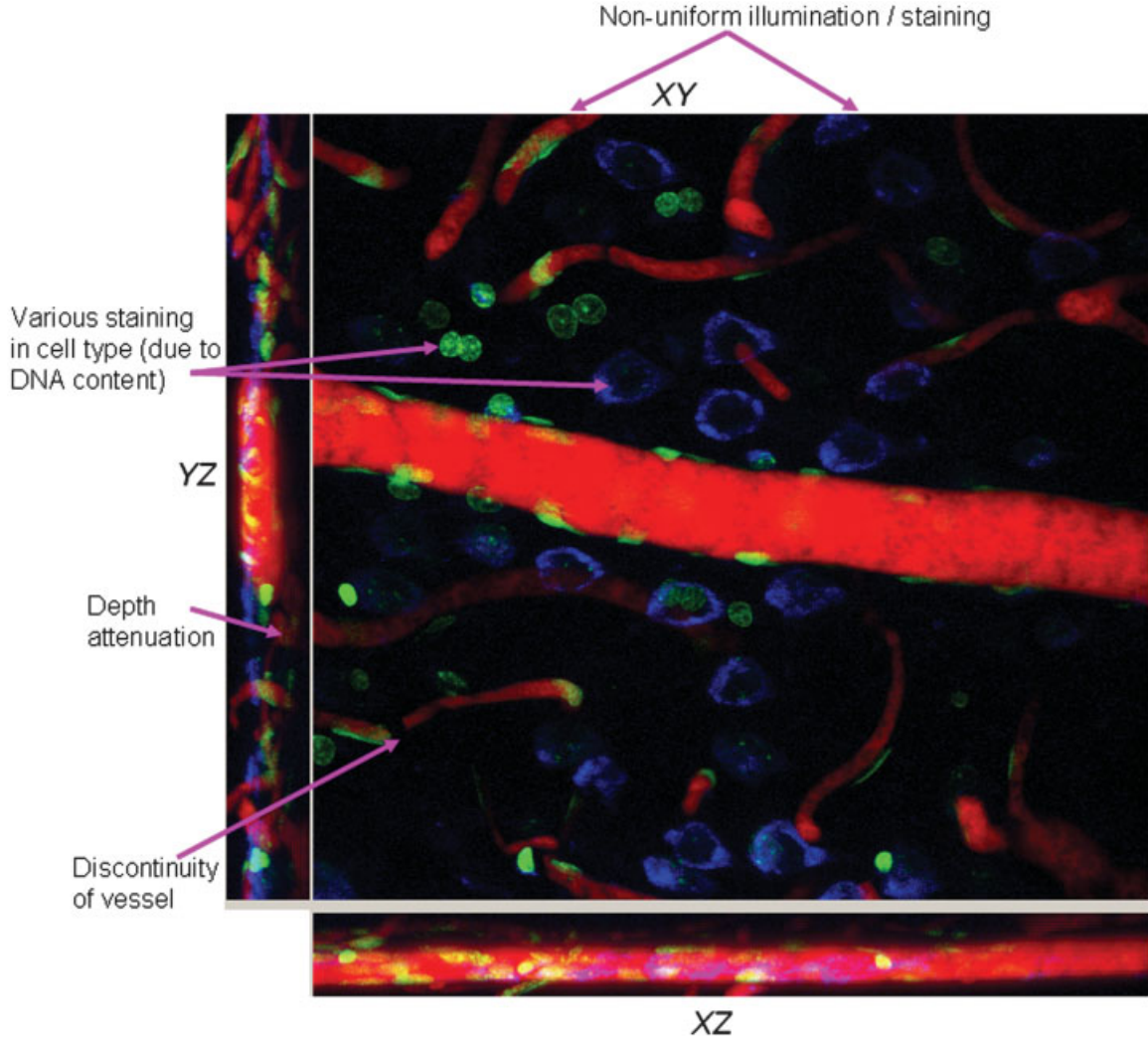


FIG. 3. Sample image illustrating the need for image preprocessing to overcome common sources of variability (marked by pink arrows) especially non-uniform staining, such as the nuclei in the left portion of the image appearing brighter than in the right portion, and apparent discontinuities in the microvasculature, depth-dependent attenuation making deeper vessels appear dimmer than others, and unequal depth-dependent attenuation of the fluorescent channels. Nuclear staining in different cell types appears nonuniform due to differences in the distribution of DNA content, and nuclear volume varies according to cell structure and activity, as evidenced by the dim, diffuse neuronal nuclei surrounded by Nissl stain and to variable attenuation. Variations in object volume, intensity, and shape are not only challenging for image analysis but also a means of categorizing different cell types.

nuclear gradients are smaller than internuclear gradients, which generally holds true. The final decision making criterion is of the following form:

$$\frac{2 \times S_{c_w}}{(S_{c_w}^1 + S_{c_w}^2)} \times \frac{(\gamma_{c_w}^1 + \gamma_{c_w}^2)}{2 \times \gamma_w} \geq \beta \quad (4)$$

where  $\beta$  is an empirically set decision threshold. This model-based merging method effectively eliminates most of the oversegmented objects by initial watershed segmentation (24). For cases of severe oversegmentation, we have described a further improved hierarchical method for performing the merging decisions that takes into account multiple connected frag-

ments at a time by relying on a region adjacency graph (26,67,68) constructed from the object fragments.

**Segmentation of the microvasculature.** Vasculature (red channel in Fig. 1) and neuronal processes are instances of tubes, which are nonuniformly deformed 3-D cylinders (22,23,30). Like blobs, these objects provide a rich set of challenges for automated image analysis systems. Tube-like objects can be filled (i.e., solid) (22,23,30,31,69) or hollow (70) in appearance. If more than one appearance model exists, a robust model-fitting algorithm can be used (71).

Two types of algorithms exist for segmenting tube-like objects: skeletonization and vectorization. Skeletonization methods work by eroding a binarized version of the image until only the innermost skeleton remains and are attrac-



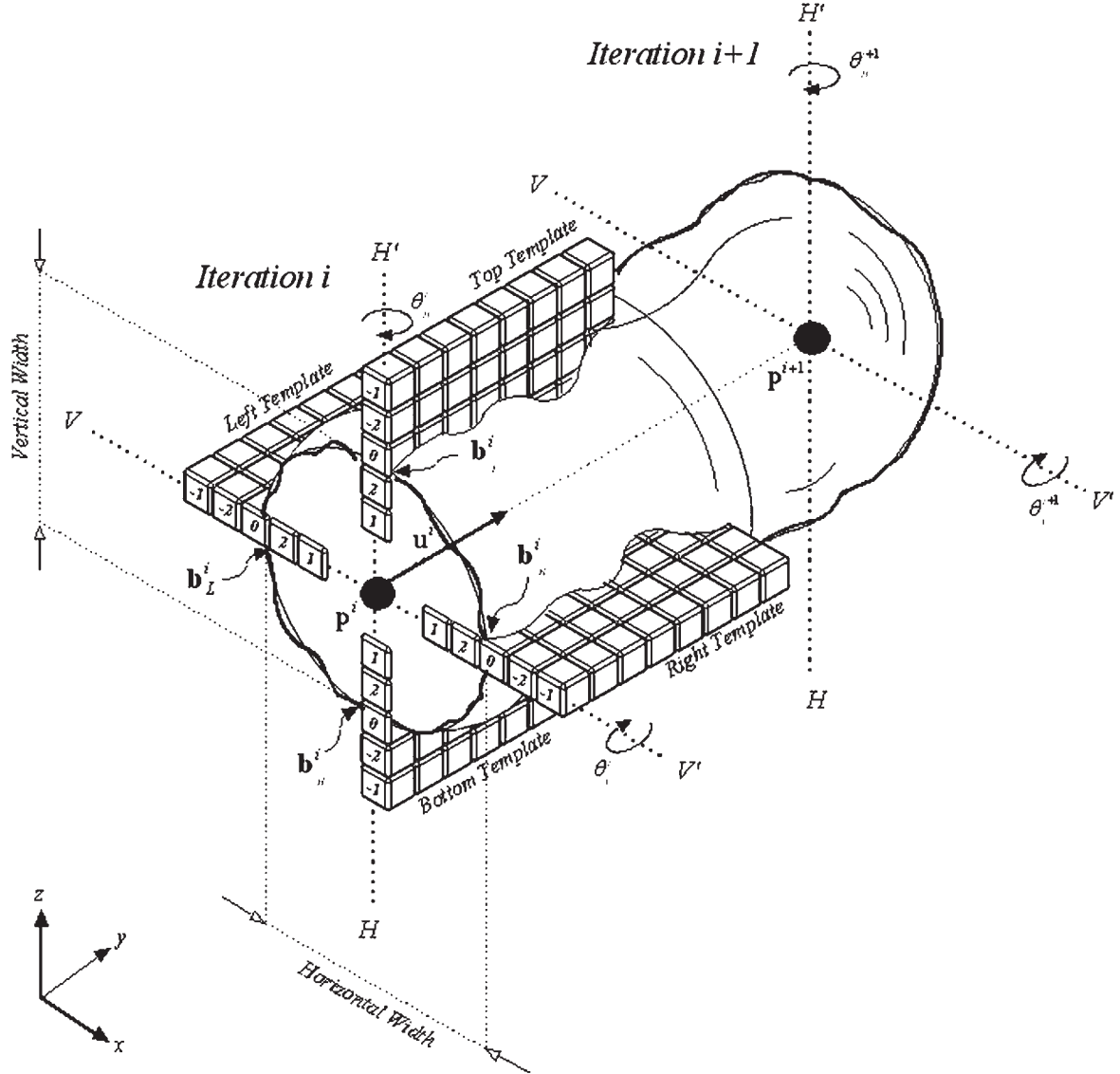


FIG. 4. The generalized cylinder modeling of the tube-like microvasculature, mathematical notation, and the templates for automated 3-D tracing. Robustness to irregularities of the object boundary relative to the straight-boundary assumption is achieved by use of the median template response.

tive when the objects are irregular, e.g., spiny neurons (72). Vectorization methods are appropriate when the objects are well modeled such as generalized cylinders (22,23,30). This method exploits more structural assumptions to better reject image clutter compared with skeletonization based methods.

For the data of interest, the strict cylinder model is relaxed to account for slight irregularities in the vasculature boundaries by incorporating a tolerance to deviations from the strict cylinder model in the software implementation. Often the microvasculature is irregular. This irregularity can be modeled by the use of robust statistics (30). This method is summarized below and illustrated diagrammatically in Figure 4.

At the core of this method is the estimation of vessel boundary locations and centerlines using a set of robust

edge detectors (22,23,30,73) that allow sequential tracing along a vessel, starting from an initial guess, a seed point, that is automatically generated. Due to intensity variations within the vasculature (e.g., as in Fig. 2), our previous method of using local 1-D maxima along rectangular grid overlaid on the image as seeds (22,23) proved unsatisfactory. This prompted us to formulate the seed detection as a vessel detection problem in 1-D using a multiscale matched-filtering method (74).

The image  $I(x)$  is decomposed into multiple scales by convolving the image with Gaussian kernels  $G_\sigma$ , where the scale, in pixels, is the Gaussian standard deviation  $\sigma$ . Edge detection is performed by taking the first derivative of the image, or precisely, the Gaussian-convolved image, to detect edges at each scale. Using the commutative properties of Gaussian convolution

and the differential operator, the image gradient at scale  $\sigma$  is calculated as  $\nabla_\sigma(x) = I(x) * (\delta G_\sigma / \delta x)$ , where  $*$  is the convolution operator. In 1-D, a vessel has two boundaries, and the next matched filtering step is formulated to detect this matching pair of boundaries, where they have opposing gradient signs. The response to this matched filter, denoted  $M_\sigma(x)$ , at pixel  $x$  and at scale  $\sigma$ , is calculated as  $M_\sigma(x) = \nabla_\sigma(x - \frac{\sigma}{2}) - \nabla_\sigma(x + \frac{\sigma}{2})$ . The multiscale response, accumulated at all scales  $[\sigma_{\min}, \sigma_{\max}]$ , is computed as  $M_{[\sigma_{\min}, \sigma_{\max}]}(x) = \max_{\sigma \in [\sigma_{\min}, \sigma_{\max}]} M_\sigma(x)$ . Also, the best scale at pixel  $x$  is  $\hat{\sigma}(x) = \arg \max_{\sigma \in [\sigma_{\min}, \sigma_{\max}]} M_\sigma(x)$ . Then, a pixel  $x$  is chosen to be a seed point if it has the maximum response  $M_{[\sigma_{\min}, \sigma_{\max}]}(x)$  around the neighborhood of scale  $\sigma(x)$ . After this 1-D seed detection performed on the rectangular-grid sampling of the image, the seeds are verified in 3-D by computing their goodness of fit with respect to the generalized cylinder model (22,23).

After seed detection, the core tracing algorithm proceeds by an update equation of the following form:

$$(\mathbf{b}^i, \mathbf{u}^i, k^i) = \arg \max_{\{(\mathbf{b}, \mathbf{u}, k) | \mathbf{b} = \mathbf{p}^i + m\mathbf{u}_\perp, m = 1, \dots, \frac{M}{2}, \mathbf{u} \in \mathbf{U}, k \in K\}} \{R(\mathbf{b}, \mathbf{u}, K)\} \quad (5)$$

where  $\mathbf{U}$  is the set of unit vectors along directions in the neighborhood of  $\mathbf{u}^i$  and  $K$  is the set of all template lengths. The vector  $\mathbf{u}$  is a unit vector along a particular 3-D angle  $\theta$ , and  $\mathbf{u}_\perp$  is the unit vector perpendicular to  $\mathbf{u}$ . The parameter  $M$  is the user-defined diameter of the widest expected vasculature. Values  $(\mathbf{b}^i, \mathbf{u}^i, k^i)$  are the results of this exhaustive search at iteration  $i$ , each representing the  $[x \ y \ z]$  location, orientation, and length, respectively, of the template that returns the maximum response  $R$ . This search is performed four times, corresponding to the four templates that make up the generalized cylinder model (Fig. 4). The corresponding template response is expressed as

$$R(\mathbf{b}, \mathbf{u}, K) = \arg \max_{k \in K} \left\{ \text{median}_{j=1 \dots k} (r(\mathbf{b} + j\mathbf{u}, \mathbf{u}_\perp)) \right\} \quad (6)$$

where  $r(\mathbf{b}, \mathbf{u}_\perp)$  is the response of a single 1-D edge detector at  $\mathbf{b}$  along the direction  $\mathbf{u}_\perp$  that is perpendicular to  $\mathbf{u}$ . Notice that a template of length  $k$  is comprised of  $k$  1-D edge detectors stacked together; hence,  $r$  is essentially a template of length 1. By using the median, the response function is robust to at most 50% of outliers (75), loosely termed as *bad edges*. Overall, this method essentially performs edge detection perpendicular to the object and averages the edge-strengths along the object boundary.

Notice that by using this method, in addition to the centerline and boundary locations, morphometric data such as length (cumulative distance between center points) and diameter (distance between boundary points) are obtained as the tracing progresses. Details are described elsewhere (22,23,30).

**Segmentation of Nissl clouds.** The diffuse cytoplasmic (Nissl) stain shown in the blue channel of Figure 1 is a good example of this class of object (24). The ability of

these objects to provide information detailing cellular and molecular structure and function, coupled with the diversity of available fluorophores and the ability of modern confocal microscopes to image multiple fluorophores, makes this an important and rapidly growing category of image analysis targets. Although these objects do not always have clear-cut geometric descriptions, they are often amenable to segmentation and quantitation by spatial association with biologically related blob-like or tube-like objects. To segment these cloud-like regions, we simply extracted the foreground by intensity thresholding after the preprocessing, followed by morphologic opening and closing, and connected component analysis to delineate the individual objects. The detected objects will be associated with the cell nuclei, which is described next.

### Individual and Interobject Feature Computation by Association

Once the microvascular tubes, nuclear blobs, and Nissl clouds are segmented from the separate channels as described above (see Fig. 5 for an example), it becomes possible to quantify the relations among these three different types of objects in a biologically informative manner. The methods are described below.

**Nuclear feature calculation.** Once segmented as described above, a wealth of nuclear morphometric data become available, including the 3-D centroidal coordinates, average intensity, volume, texture and shape factor, etc. Table 1 shows a fragment of such a morphometric summary that is routinely generated by the blob segmentation software described in previous work (24–26). Given the nonstoichiometric nature of the dyes used, the absence of calibration targets, and depth-dependent attenuation, we emphasize the use of measurements of spatial factors over the fluorescent intensity values. If the fluorescence signal can be made quantitative, these features can also be exploited in a direct manner.

The size and shape of the nuclei allow further discrimination of cell types. The nuclear volume is the total number of voxels in a segmented nucleus. The shape factor measures how spherical an object (blob) is and is defined mathematically as:  $S = (9 \times |\mathbf{b}|^3) / (1,024 \times \pi \times V^2)$ , where  $\mathbf{b}$  denotes the surface voxels of an object and  $V$  is the volume of the object. Notice that  $S$  usually takes a value between 0 and 1. The closer this number is to 1, the closer the object is to a sphere. This feature can be used to distinguish the types of nuclei in the image. For example, normal neurons tend to be spherical, and endothelial cells are more slim and elliptical.

Texture measurement reflects the uniformity of the chromatin, as reflected by the intensity of nuclear voxels. There are several ways to quantify texture. The simplest one is the variation of intensity value among all nuclear voxels, i.e.,  $T = \sigma(I[\mathbf{X}_o])$ , where  $\sigma$  stands for the standard deviation operator and  $I(\mathbf{X}_o)$  denotes the intensity of the object voxels. The more sophisticated texture can be defined by the second-order histogram of the intensity values (co-occurrence matrix). It is obviously more com-



Fig. 5. Intra- and interobject measurements. **a:** Nuclei are outlined in white and numbered in white (class 0; non-neuronal) or red (class 1; neuronal). The vessel centerline traces are shown in yellow. The distance from each nucleus to the nearest vessel is indicated by a white line. Nuclei that are closer to an edge of the image than they are to the nearest vessel are excluded. **b:** Sample 3-D graphic rendering of the same data allows improved visualization by perspective and interactive manipulation of view-point.

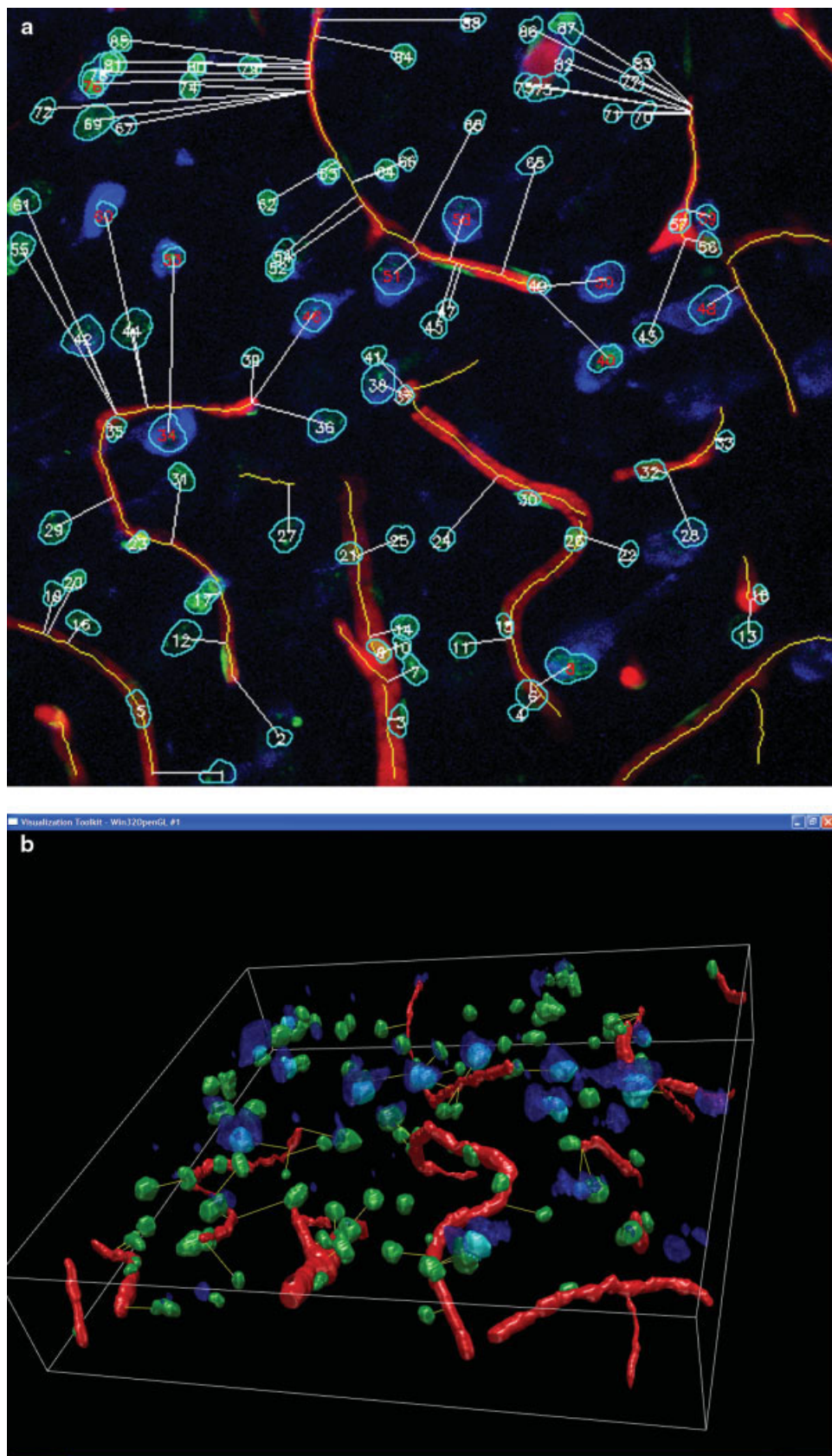


Table 1  
A Partial Tabular Output Corresponding to Figure 5\*

Nuclear ID	X	Y	Z	Intensity	Volume	Texture	Shape factor	Class	Nissl volume	Distance to vessel	Vessel diameter
1	122	13	25	9	350	4.12	0.70	0	0	72.86	4.24
2	75	20	14	52	655	14.02	0.77	0	0	35.61	4.24
3	272	22	17	34	1,430	22.67	0.80	0	0	27.95	16.53
4	243	25	36	14	681	8.06	0.68	0	0	13.82	10.82
5	137	35	21	9	640	7.79	0.79	0	0	76.58	4.24
6	301	36	13	80	1,473	39.17	0.81	0	0	14.25	12.10
7	177	38	9	25	1,934	25.42	0.81	0	0	67.19	10.82
8	348	43	15	16	344	9.73	0.68	0	0	4.43	16.28
9	233	44	24	14	1,290	12.46	0.74	0	0	19.07	8.36
10	17	45	11	22	1,518	20.79	0.77	0	0	20.43	6.08
11	433	64	11	27	1,141	16.36	0.73	0	0	8.22	4.26
12	374	69	18	9	557	7.68	0.75	0	0	34.37	5.66
13	109	71	6	27	2,169	19.58	0.73	1	6084	49.02	4.24
14	406	80	15	60	378	13.19	0.71	0	0	2.88	3.61
15	449	82	12	41	534	16.47	0.70	0	0	27.34	3.61

\*Standard nuclear features such as 3-D location, average intensity, volume, texture and shape factor and associative interobject features such as the distance of each nucleus to the vasculature are included. The nuclear classification result is shown by the Class column, where 1 and 0 stand for nuclei with and without the Nissl stain, respectively. The (x, y, z, volume) measurements are in voxel units. The distances to vessels and vessel diameters are in micrometers.

putationally intensive. We used the first method after attenuation correction of the nuclear channel.

**Vascular feature computation.** Although a rich set of vascular measurements is collected by the tracing software during the tracing operations as described in the previous section, only the simplest of these were used in this work. These included the location of centerline points, the boundary surface of the vessels, and local widths and direction vectors at each of the centerline points.

**Associations between the nuclei and the Nissl cytoplasmic stain.** In analyzing the nuclear (CyQuant) data, we were interested in being able to distinguish neurons from endothelial cells on the basis of their morphology and proximity to Nissl substance (clouds) or neurovasculature (tubes), respectively. The cellular diversity encountered in the rat neocortex produced a range of nuclear profiles with marked differences in morphology and staining intensity. Preliminary assessment of the neuronal count indicated that many highly active neuronal nuclei displaying poor, heterogeneous CyQuant labeling were not detected by the software, even when the threshold was set so low that false positives (artifacts) were being counted.

From a software analysis standpoint, the Nissl clouds essentially surround the nuclei, or exist in close proximity. Each voxel in the Nissl cloud was associated with the nearest nucleus based on its Euclidean distance from the nuclear surface (25). This allows the nuclei in the image to be classified into two broad categories based on whether or not they are associated with the Nissl stain. Specifically, if the total intensity of Nissl signals in the region of interest (a shell with certain thickness surrounding nucleus) exceeds a prespecified threshold, we deem the nucleus as Nissl positive; thus, the corresponding cell is a neuron. An unavoidable challenge, noted above, is the differential attenuation of the Nissl stain from that of nuclear Cyquant stain. In general, a more rapid attenuation of the nuclear stain compared with the cytoplasmic

stain results in invisible “ghost” nuclei that must be inferred from the missing part of the cytoplasmic stain. In contrast, a more rapid attenuation of the cytoplasmic stain results in fewer detections of nuclei that are actually associated with the cytoplasmic stain. The depth-dependent attenuation correction and adaptive thresholding of the Nissl signal were helpful in minimizing such sources of error.

**Associations between the nuclei and the microvasculature.** Each nucleus was simply associated with the closest point on the vasculature as measured by its Euclidean distance from the centroid of the nucleus to the estimated surface of the vessel segment. Measuring the distance to the surface, as opposed to the centerline, allows compensation for the variable thickness (bore) of the microvasculature and allows simple identification of cells that are closely associated with the microvasculature (e.g., endothelial cells). In addition, the distances of the cells from the microvasculature are biologically significant because the nutrient and oxygen levels of cells are directly affected by proximity to a microvessel. If the cell membrane is labeled separately, it is also possible, in principle, to quantify its distance to the microvascular surface.

## RESULTS

### Manual Validation of the Image Analysis

The main objective of this analysis was to quantify the disagreement between automated and manually inspected results where a measurement of the disagreements is interpreted as the error. The manually inspected results have a large subjective component and, therefore, are prone to inter- and intraobserver variabilities. For blobs and clouds, errors include false detection (false positives), misses (false negatives), erroneous separation of connected objects (hypersegmentation), and errors in correctly delineating the boundaries of objects (24). In terms of classification, objects can be misidentified; in most

cases this error can be reduced by careful evaluation, refinement, and use of identifying criteria. For tube-like objects, errors include falsely traced segments and branch points (false positives) and missed segments and branch points (false negatives), accuracy of the trace, accuracy of width measurements, and accuracy in locating branching/crossover points (76,77).

Quantitative validation may also involve voxel-to-voxel comparisons of the segmented volume or comparisons of any other entities derived from the segmented volume such as the vasculature centerline or the cell centroid. The comparison can be performed automatically to further reduce the subjectivity of validating the segmentation results (22,23). In the case of tube-like objects, the centerline locations are extremely important because almost all morphometrics depend on them. Centerline locations are typically validated for the deviation from a "true" centerline, which reflects the accuracy of the automated method, and the centerline coverage of the objects in the image, which reflects how much manual editing the automated result needs.

Manual validation was performed on two datasets to confirm the accuracy of automated nuclear counting and neuronal and endothelial cell classification. Validation of automated categorization of cells was accomplished by manually reviewing the automated output of the 3-D datasets one optical section at a time. Neuronal nuclei were identified because of their close association with Nissl-stained clouds. Endothelial cell nuclei were identified by their nuclear morphology and close apposition to vascular elements in 2-D projections and 3-D datasets. The "other cells" category includes all cells that did not meet either of the above criteria for categorization and includes astrocytes, microglia, oligodendrocytes, smooth muscle cells, and pericytes. In addition, cases of under- and hypersegmentation were scored. Erroneous boundary detection was not substantial except for a few instances where one object encroached on an immediately adjacent object and therefore was not otherwise noted. In a representative dataset, the software identified 115 nuclei (blobs); 107 were detected through manual validation. Of these 107 nuclei, 5 (4.7%) were missed, 2 (1.9%) were involved in a substantial encroachment, 10 (9.3%) were hypersegmented to appear as 23 nuclei, and 4 (3.7%) were undersegmented to appear as 2 nuclei. In general, the missed and hypersegmented nuclei had diffuse labeling: thus, these presented a serious challenge to the image analysis software. Most organs do not display such a pronounced difference in nuclear morphology; indeed, nervous tissue, because of the variety of cells, e.g., large and small neurons, various glia, and endothelial cells, and testis, because of cells with different ploidy, e.g., Sertoli cells and developing spermatogonia, are among the most challenging tissues encountered in this regard.

Data are presented to describe the measured distance between neuron, endothelial cell, and other cell nuclei and the edge of the nearest blood vessel (Fig. 6). Comparison of data from automatically categorized (Fig. 6A,C) and manually validated (Fig. 6B,D) nuclei demonstrates a high degree of accuracy and good agreement between the auto-

mated analysis and manual validation. In both datasets, the endothelia are easily distinguished by their location relative to the neurovasculature, whereas the neurons and other cells share a similar distribution. In the first dataset (Fig. 6A,B) the mean distance  $\pm$  standard deviation of the centroid of neuronal nuclei from the nearest vessel is  $13.3 \pm 7.1 \mu\text{m}$  (automated) or  $14.7 \pm 7.4 \mu\text{m}$  (validated), whereas the mean distance of "other" cells is  $16.6 \pm 5.8 \mu\text{m}$  (automated) or  $15.9 \pm 6.4 \mu\text{m}$  (validated). Endothelial cell nuclei average  $-0.4 \pm 2.5 \mu\text{m}$  (automated) or  $-0.2 \pm 3.8 \mu\text{m}$  (validated) from the nearest vessel wall. In the second dataset (Fig. 6C,D) the mean distance of neurons from the nearest vessel is  $10.0 \pm 6.4 \mu\text{m}$  (automated) or  $10.5 \pm 6.3 \mu\text{m}$  (validated), whereas the mean distance of "other" cells is  $11.4 \pm 5.3 \mu\text{m}$  (automated) or  $10.0 \pm 5.6 \mu\text{m}$  (validated). Endothelial cell nuclei average  $-0.6 \pm 1.8 \mu\text{m}$  (automated) or  $-0.1 \pm 2.2 \mu\text{m}$  (validated) from the nearest vessel wall. The differences between values for each dataset likely reflect differences in the organization of the NVU in different cortical regions. None of the differences between automatically categorized and manually validated datasets were statistically significant when compared using a two-tailed Student's paired *t* test ( $P = 0.48$  for dataset 1 neurons, 0.38 for dataset 1 other, 0.83 for dataset 1 endothelia, 0.26 for dataset 2 neurons, 0.72 for dataset 2 other, and 0.41 for dataset 2 endothelia).

Several cases of misidentification occurred when a neighboring glial cell was immediately adjacent to a neuron and was therefore placed in the Nissl-positive category. Resolving such ambiguities in a general manner requires further investigation.

Figure 7 shows an example indicating the correlation of the distance between the calculated volume of each nucleus and its nearest neighboring vascular element for two datasets. Comparisons of automatically identified nuclei (solid symbols) and validated observations (open symbols) demonstrate the accuracy of object detection. The primary source of error was hypersegmentation of nuclei, as indicated by several unvalidated smaller nuclei (e.g., numbered solid symbols). These smaller objects were manually grouped as indicated by the appearance of larger validated nuclei (e.g., numbered open symbol). Endothelial cells had some of the smallest nuclear volumes. Interestingly, neurons with larger nuclear volumes were only located farther from vascular elements, whereas neurons with smaller nuclear volumes exhibited a more variable distribution. Other cell types (astrocytes, microglia, smooth muscle cells, and pericytes) were also uniformly distributed; therefore, distinguishing these different cell populations will require additional techniques (Nissl staining, immunohistochemical labeling of specific glial markers, etc.). The distribution of astrocytes may result from their roles in blood-brain barrier function, synaptic transmission, and metabolic support (78,79). In addition, microglia are likely to be uniformly dispersed throughout the cortex. Studies using additional histochemical or immunohistochemical markers to label astrocytes and microglia will further delineate the distribution



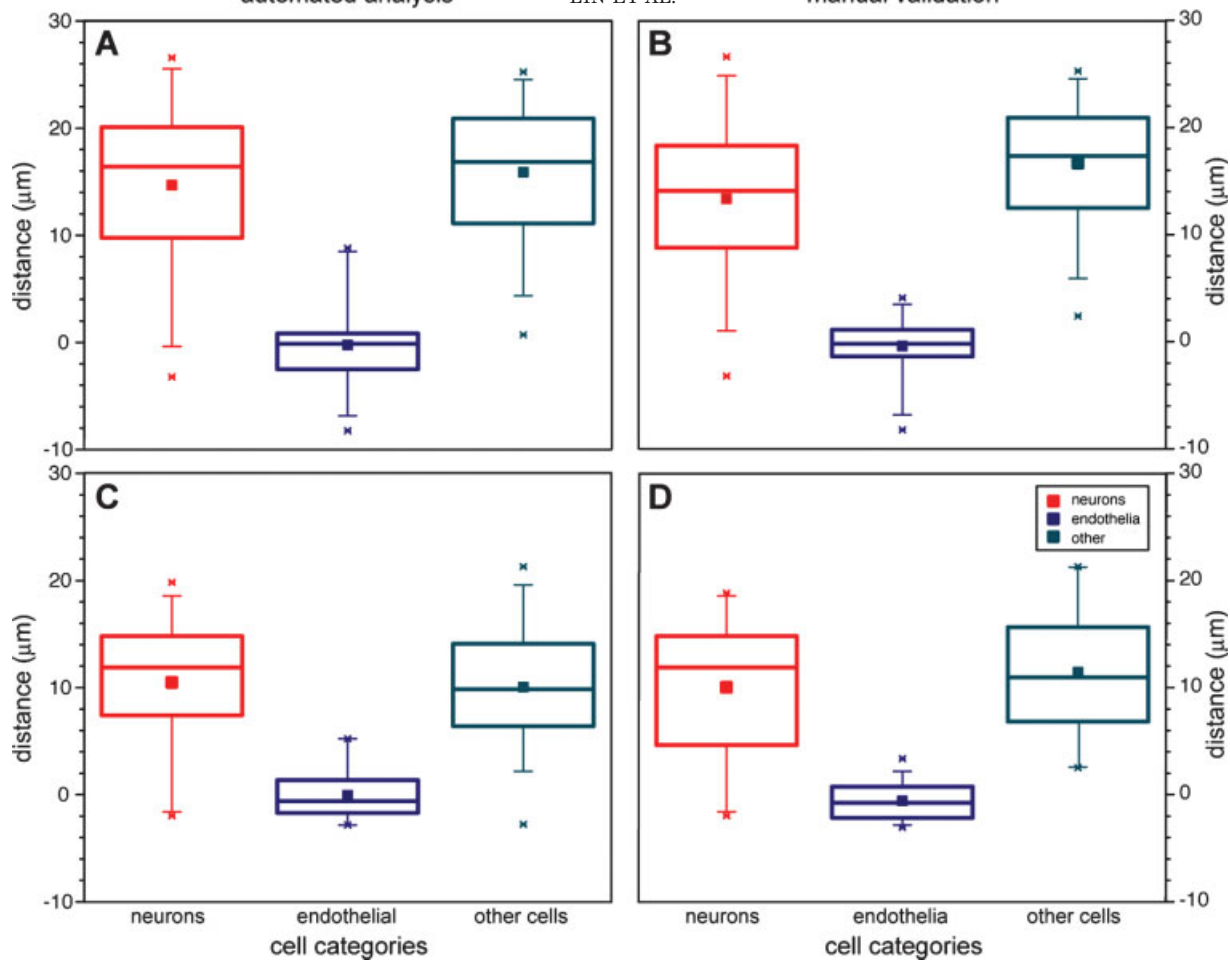


FIG. 6.

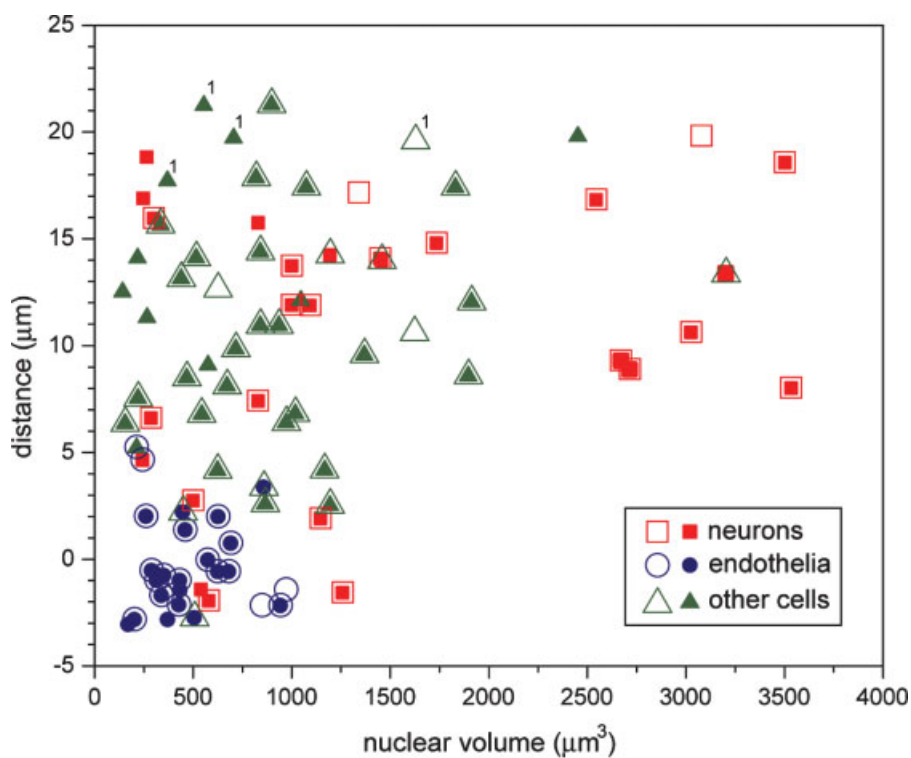


FIG. 7. Correlation of the distance between the calculated volume of each nucleus and its nearest neighboring vascular element. Comparison of automatically identified nuclei (solid symbols) and validated observations (open symbols) demonstrate the accuracy of object detection. The primary source of error was hypersegmentation. This is illustrated by the smaller automatically detected nuclei (numbered 1 beside solid symbols, upper right) and the larger validated nucleus (indicated by open symbols labeled with 1). The latter represents the sum of the former. Nuclei were categorized as described in Figure 6. Data are the same data plotted in Figures 6A and 6B.

of these cells and will provide functional information to define their roles in the NVU under normal and pathologic conditions.

## DISCUSSION AND CONCLUSIONS

We have presented a “divide and conquer” strategy for detailed and scalable analysis of complex biological systems using the neurovascular unit as examples. Separately imaging multiple structural and functional entities in the system using multiple fluorescent markers together with innovative specimen preparation approaches results in a set of “pure channels” each of which contains only one type of cytological object. In the examples shown, channel purity was achieved by simple means. When more complex fluorophores with overlapping spectral bands are used, the use of spectral unmixing software would be necessary (16,80). The experiments shown here can be expanded to larger-scale studies. In future work, one can include larger numbers of channels describing more sets of structural and functional components. Although not demonstrated here, this approach, in principle, allows combinatoric labeling and analysis of large numbers of such entities using a modest number of fluorophores. Recent advances such as quantum dots (81) can be expected to further accelerate this potential.

The software strategy is driven by the availability of pure channels. By integrating separately developed 3-D image analysis tools for different types of cytological objects, it is possible to attempt a more detailed analysis of complex biological systems such as the NVU. This advance was made possible by integration of our diverse image analysis tools, especially high-quality blob and tube segmentation codes. By using key objects, especially the cell nuclei and the microvascular segments, as a spatial anchor/reference, it was possible to quantify a potentially unlimited number of fluorophore signals by association analysis. Indeed, combinatoric association analysis is the logical “glue” that serves as a powerful yet biologically meaningful integrative principle. The NVU example presented in this work represents the simplest instance of such analysis.

The resin casts of the neurovasculature provided a unique set of challenges for the image analysis software. The rhodamine B-doped resin displayed some heterogeneous stain distribution that made determination of initial seed points challenging. Using local maxima of 1-D intensity profiles from rectangular grids as in our previous method of seed point detection (22,23) produced

seed points located close to vessel boundary rather than at the vessel centerline. By reformulating the seed point detection as a multiscale matched filter (74) to detect the presence of the lumen of the generalized-cylinder model (Fig. 4) in 1-D, we were able to obtain the desired seed point placements. The tracing algorithms from previous work (22,23,30) were adequate after this enhancement.

The vascular cast datasets used in this study presented a unique set of challenges for quantitation. Many of the values we obtained for blood vessel diameters were between 1 and 2  $\mu\text{m}$ , smaller than the average 4 to 5  $\mu\text{m}$  commonly reported in other casting studies (82). These values are not likely due to difficulties in setting threshold values to recognize the entire vessel during analysis because manual validation confirmed that the traced boundaries of vascular elements are reasonably accurate. Rather, these data seem to reflect a shortcoming in the vascular casting technique at this time. Indeed, scanning electron microscopic analysis of corrosion casts using these same tissue samples has revealed that many of the smaller vessels are incompletely filled, often appearing collapsed (data not shown). Subsequent studies in our laboratory have identified changes to buffer composition and have led to pressure perfusion protocols that significantly improve cast quality. The ability of our analysis to identify a potential procedural issue that we could confirm using scanning electron microscopy underscores the strength of this technique.

Some of the observed nuclear undersegmentation may be due to the relatively large Z-step size used for this study. The 1- $\mu\text{m}$  steps were chosen instead of 0.375  $\mu\text{m}$  (which would match the X and Y resolutions) because they appeared during image collection to provide adequate vertical resolution and reduce the effects of photobleaching, which were especially noticeable with the Nissl stain. In addition, HBHS was selected as a mounting medium over glycerin in an attempt to avoid tissue shrinkage and preserve the relation between tissue and the vascular cast and to quickly transition to the aqueous alkaline solutions necessary to prepare corrosion casts. As a result, the tissue was not cleared, and fluorescence signal may have been scattered and attenuated more than usual. Data generated using more conventional techniques will likely generate fewer anomalies. We are currently developing tissue preparation and image analysis strategies to address these challenges.

The life-sciences researcher is often able to perform some types of automated 2-D image analysis and, occasion-

Fig. 6. Validation of automated measurements for descriptions of cell distributions around vasculature elements in rat neocortex. **A, C:** Data obtained by automated analyses demonstrate measured distances between neurons (red graphic elements), endothelial cells (blue graphic elements), and other cells (green graphic elements). **B, D:** Data validated by manual inspection of individual optical sections for each dataset demonstrate the accuracy of the automated analysis. These are representative of datasets collected from two of eight randomly selected samples from rat cortex. Neuronal nuclei were identified because of their close association with Nissl-stained clouds. Endothelial cell nuclei were identified by their close apposition to vascular elements. The “other cells” category includes all cells for which there were insufficient criteria for categorization, e.g., astrocytes, microglial, and neuronal nuclei that did stain with Nissl. From top to bottom of each column of data, the symbols represent the maximum data value (x), 95th percentile (top of line), 75th percentile (top of box), median (line), mean (square), 25th percentile (bottom of box), 5th percentile (bottom of line), and minimum data value (x). The numbers of nuclei included in this analysis were 21, 19, 24, and 39 for neurons, 25, 21, 36, and 56 for endothelia, and 33, 33, 60, and 76 for other cells in A, B, C, and D, respectively.

ally, 3-D analysis using off-the-shelf software, e.g., NIH Image, MetaMorph by Universal Imaging, and VoxellView by Vital Images. The higher complexity and integration level of the analysis described here and the current state of evolution of automated 3-D image analysis technology imply that the assistance of an image analysis specialist is often called for. The study presented here benefited from active cross-disciplinary collaboration among life-sciences researchers and computational scientists. Further, the availability of multiple types of segmentation routines within the same research group proved to be a significant advantage in this integrative study. The seemingly informal terminology presented here (blobs, tubes, clouds, etc.) was valuable in bridging across disciplines. The proposed division of the overall image analysis task by these object types also forms a solid basis for facilitating productive discussion between life-sciences researchers and computer scientists.

Quantitative image analysis is a broadly applicable approach with specific benefits to investigations of the NVU. By facilitating the identification of different central nervous system cell types relative to one another and the neurovasculature, this software allows us to explore how these interactions change in different brain regions and in response to disease or injury. The ability to characterize multiple biological elements with markedly different characteristics (e.g., tubes, clouds, blobs) and discriminate subtle differences in conserved features (blob classification) is essential to the study of the NVU.

### LITERATURE CITED

1. Park J, Choi K, et al. Coordinated interaction of the vascular and nervous systems: from molecule- to cell-based approaches. *Biochem Biophys Res Commun* 2003;311:247-253.
2. Zonta M, Angulo M, et al. Neuron-to-astrocyte signaling is central to the dynamic control of brain microcirculation. *Nat Neurosci* 2003;6:43-50.
3. del Zoppo G. Microvascular changes during cerebral ischemia and reperfusion. *Cerebrovasc Brain Metab Rev* 1994;6:47-96.
4. Yoder E. Modifications in astrocyte morphology and calcium signaling induced by a brain capillary endothelial cell line. *Glia* 2002;38:137-145.
5. Simard M, Arcuino G, et al. Signaling at the gliovascular interface. *J Neurosci* 2003;23:9254-9262.
6. Cox S, Woolsey T, et al. Localized dynamic changes in cortical blood flow with whisker stimulation corresponds to matched vascular and neuronal architecture of rat barrels. *J Cereb Blood Flow Metab* 1993;13:899-913.
7. Woolsey T, Rovainen C, et al. Neuronal units linked to microvascular modules in cerebral cortex: response elements for imaging the brain. *Cereb Cortex* 1996;6(5).
8. del Zoppo G, Mabuchi T. Cerebral microvessel responses to focal ischemia. *J Cereb Blood Flow Metab* 2003;23:879-894.
9. Kitano H. Systems biology: a brief overview. *Science* 2002;295:1662-1664.
10. Kohane IS, Kho AT, et al. Microarrays for an integrative genomics. Cambridge: MIT Press; 2003.
11. Shapiro HM. Practical flow cytometry. New York: Wiley-Liss; 2003.
12. Pawley JB. Handbook of biological confocal microscopy. New York: Plenum Press; 1995.
13. Sheppard C, Shotton D, et al. Confocal laser scanning microscopy. Oxford, UK: BIOS Scientific Publishers/New York: Springer; 1997.
14. Diaspro A. Confocal and two-photon microscopy: foundations, applications, and advances. New York: Wiley-Liss; 2002.
15. Matsumoto B. American Society for Cell. Cell biological applications of confocal microscopy. Amsterdam: Academic Press; 2002.
16. Dickinson M, Bearman G, et al. Multi-spectral imaging and linear unmixing add a whole new dimension to laser scanning fluorescence microscopy. *Biotechniques* 2001;31:1272-1278.
17. Zimmermann T, Rietdorf J, et al. Spectral imaging and linear unmixing enables improved FRET efficiency with a novel GFP2-YFP FRET pair. *FEBS Lett* 2002;531:245-249.
18. Zimmermann T, Rietdorf J, et al. Spectral imaging and its applications in live cell microscopy. *FEBS Lett* 2003;546:87-92.
19. Valeur B. Molecular fluorescence: principles and applications. Weinheim: Wiley-VCH; 2002.
20. Becker DE, Ancin H, et al. Automated 3-D montage synthesis from laser-scanning confocal images: application to quantitative tissue-level cytological analysis. *Cytometry* 1996;25:235-245.
21. Beck JC, Murray JA, et al. Computer-assisted visualizations of neural networks: expanding the field of view using seamless confocal mounting. *J Neurosci Methods* 2000;98:155-163.
22. Al-Kofahi KA, Lasek S, et al. Rapid automated three-dimensional tracing of neurons from confocal image stacks. *IEEE Trans Inf Technol Biomed* 2002;6:171-187.
23. Al-Kofahi O, Can A, et al. Multi-view three-dimensional image mounting & signal attenuation correction for maximizing the imaging depth and lateral extent of confocal microscopes. *Microsc Microanal* 2002, Volume 8, pp. 1042CD-1044CD.
24. Lin G, Adiga U, et al. A hybrid 3D watershed algorithm incorporating gradient cues and object models for automatic segmentation of nuclei in confocal image stacks. *Cytometry* 2003;56A: 23-36.
25. Chawla MK, Lin G, et al. 3D-catFISH: a system for automated quantitative three-dimensional compartmental analysis of temporal gene transcription activity imaged by fluorescence in situ hybridization. *J Neurosci Methods* 2004;139:13-24.
26. Lin G, Chawla MK, et al. Hierarchical, model-based merging of multiple fragments for 3-D segmentation of nuclei. *Cytometry* 2004;63A: 20-33.
27. Cohen AR, Roysam B, et al. Automated tracing and volume measurements of neurons from 3-D confocal fluorescence microscopy data. *J Microsc* 1994;173:103-114.
28. Can A, Shen H, et al. Rapid automated tracing and feature extraction from retinal fundus images using direct exploratory algorithms. *IEEE Trans Inf Technol Biomed* 1999;3:125-138.
29. Can A, Stewart CV, et al. A feature-based, robust, hierarchical algorithm for registering pairs of images of the curved human retina. *IEEE Trans Pattern Anal Mach Intell* 2002;24:347-364.
30. Abdul-Karim M-A, Al-Kofahi K, et al. Automated tracing and change analysis of angiogenic vasculature from in vivo multiphoton confocal image time series. *Microvasc Res* 2003;66:113-125.
31. He W, Hamilton TA, et al. Automated three-dimensional tracing of neurons in confocal and brightfield images. *Microsc Microanal* 2003; 9:296-310.
32. Olson K. Preparation of fish tissues for electron microscopy. *J Electron Microsc Tech* 1985;2:217-228.
33. Castenholz A. Examination of injected specimens by confocal laser scanning microscopy and scanning electron microscopy. *Scanning Microsc* 1995;9:1245-1254.
34. Adiga U, Chaudhuri B. An efficient method based on watershed and rule-based merging for segmentation of 3D histo-pathological images. *Pattern Recogn* 2001;34:1449-1458.
35. Adiga U, Chaudhuri B. Some efficient methods to correct confocal images for easy interpretation. *Micron* 2001;32:363-370.
36. Can A, Al-Kofahi O, et al. Attenuation correction in confocal laser microscopes: a novel two-view approach. *J Microsc* 2003;211: 67-79.
37. Russ JC. The image processing handbook. Boca Raton, FL: CRC Press; 1994.
38. Castleman K. Digital image processing. Englewood Cliffs, NJ: Prentice-Hall; 1996.
39. Serra JP, Soille P. Mathematical morphology and its applications to image processing. Dordrecht: Kluwer Academic Publishers; 1994.
40. Bovik AC, Aggarwal SJ, et al. Automatic area and volume measurements from digital biomedical images. In: Häder D-P, editor. Image analysis: methods and applications. Boca Raton, FL: CRC Press; 2001. p 23-64.
41. Sato Y, Nakajima S, et al. Three-dimensional multi-scale line filter for segmentation and visualization of curvilinear structures in medical images. *Med Image Anal* 1998;2:143-168.
42. Roysam B, Lin G, et al. Automated 3-d image analysis methods for confocal microscopy. In: Pawley J, editor. Handbook of confocal microscopy. New York: Plenum Press; 2004.
43. Netten H, Young IT, et al. FISH and chips: automation of fluorescent dot counting in interphase cell nuclei. *Cytometry* 1997;28:1-10.
44. Solórzano COD, Santos A, et al. Automated FISH spot counting in interphase nuclei: statistical validation and data correction. *Cytometry* 1998;31:93-99.



45. Adiga PSU, Chaudhuri BB. Efficient cell segmentation tool for confocal microscopy tissue images and quantitative evaluation of FISH signals. *Microsc Res Tech* 1999;44:49–68.
46. Castleman KR, White BS. Dot count proportion estimation in FISH specimens. *Bioimaging* 2001;3:88–93.
47. Sunil Kumar K, Desai UB. Joint segmentation and image interpretation. *Pattern Recogn* 1999;32:577–589.
48. Neumann A. Graphical Gaussian shape models and their application to image segmentation. *IEEE Trans Pattern Anal Mach Intell* 2003;25:316–329.
49. Zucker SW. Region growing: childhood and adolescence. *Comput Vis Graph Image Process* 1976;5:382–399.
50. Besl PJ, Jain RC. Segmentation through variable-order surface fitting. *IEEE Trans Pattern Anal Mach Intell* 1988;10:167–192.
51. Adams R, Bischof L. Seeded region growing. *IEEE Trans Pattern Anal Mach Intell* 1994;16:641–647.
52. Trucco E, Fisher RB. Experiments in curvature-based segmentation of range data. *IEEE Trans Pattern Anal Mach Intell* 1995;17:177–182.
53. Zhu SC, Yuille A. Region competition: unifying snakes, region growing, and Bayes/MDL for multiband image segmentation. *IEEE Trans Pattern Anal Mach Intell* 1996;18:884–900.
54. Blake A, Zisserman A. Visual reconstruction. Cambridge: MIT Press; 1987.
55. Black MJ, Rangarajan A. On the unification of line processes, outlier rejection, and robust statistics with applications in early vision. *Int J Comput Vis* 1996;19:57–91.
56. Xu Y, Oberbacher EC. 2D image segmentation using minimum spanning trees. *Image Vis Comput* 1997;15:47–57.
57. Shi J, Malik J. Normalized cuts and image segmentation. *IEEE Trans Pattern Anal Mach Intell* 2000;22:888–905.
58. Guigues L, Le Men H, et al. The hierarchy of the cocoons of a graph and its application to image segmentation. *Pattern Recogn Lett* 2003;24:1059–1066.
59. Vincent L, Soille P. Watersheds in digital spaces: an efficient algorithm based on immersion simulations. *IEEE Trans PAMI* 1991;3(6).
60. Ancin H, Roysam B, et al. Advances in automated 3-D image analyses of cell populations imaged by confocal microscopy. *Cytometry* 1996;25:221–234.
61. Malpica N, de Solorzano CO, et al. Applying watershed algorithms to the segmentation of clustered nuclei. *Cytometry* 1997;28:289–297.
62. Solorzano C, Rodriguez E. Segmentation of confocal microscope images of cell nuclei in thick tissue sections. *J Microsc* 1999;193:212–226.
63. Pavlidis T, Liow Y-T. Integrating region growing and edge detection. *IEEE Trans Pattern Anal Mach Intell* 1990;12:225–233.
64. Shafarenko L, Petrou M, et al. Automatic watershed segmentation of randomly textured color images. *IEEE Trans Image Process* 1997;6:1530–1544.
65. Wahlby C, Bengtsson E. Segmentation of cell nuclei in tissue by combining seeded watersheds with gradient information. In: Bigun J, Gustavsson T, editors. *Lecture notes in computer science*. Volume 2749. New York: Springer-Verlag; 2003. p 408–414.
66. Borgefors G. Distance transformations in digital images. *Comput Vis Graph Image Process* 1986;34:344–371.
67. Ballard DH, Brown CM. Computer vision. Englewood Cliffs, NJ: Prentice-Hall; 1982.
68. Wu X. Adaptive split-and-merge segmentation based on piecewise least-square approximation. *IEEE Trans Pattern Anal Mach Intell* 1993;15:808–815.
69. Meijering E, Jacob M, et al. Design and validation of a tool for neurite tracing and analysis in fluorescence microscopy images. *Cytometry* 2004;58A:167–176.
70. Weichert F, Müller H, et al. Virtual 3D IVUS vessel model for intravascular brachytherapy planning. I. 3D segmentation, reconstruction, and visualization of coronary artery architecture and orientation. *Med Phys* 2003;30:2530–2536.
71. Mahadevan V, Narasimha-Iyer H, et al. Robust model-based vasculature detection in noisy biomedical images. *IEEE Trans Inf Technol Biomed* 2004;8:360–376.
72. Koh Y, Lindquist WB, et al. An image analysis algorithm for dendritic spines. *Neural Comput* 2002;14:1283–310.
73. Sun Y, Lucariello RJ, et al. Directional low-pass filtering for improved accuracy and reproducibility of stenosis quantification in coronary arteriograms. *IEEE Trans Med Imaging* 1995;14:242–248.
74. Kay SM. Fundamentals of statistical signal processing. Englewood Cliffs, NJ: Prentice-Hall; 1993.
75. Huber PJ. Robust statistics. New York: Wiley; 1981.
76. Abu-Tarif AA, Ahmad A. Volumetric registration based on intensity and geometry features (PhD thesis). Troy, NY: Rensselaer Polytechnic Institute; 2002.
77. Al-Kofahi KA, Can A, et al. Median-based robust algorithms for tracing neurons from noisy confocal microscope images. *IEEE Trans Inf Technol Biomed* 2003;7:302–317.
78. Nedergaard M, Ransom B, et al. New roles for astrocytes: redefining the functional architecture of the brain. *Trends Neurosci* 2003;26:523–530.
79. Newman EA. New roles for astrocytes: regulation of synaptic transmission. *Trends Neurosci* 2003;26:536–542.
80. Sinclair MB, Timlin JA, et al. Design, construction, characterization, and application of a hyperspectral microarray scanner. *Appl Optics* 2004;43:2079–2088.
81. Jaiswal JK, Mattoussi H, et al. Long-term multiple color imaging of live cells using quantum dot bioconjugates. *Nat Biotechnol* 2003;21:47–51.
82. Hossler F, Douglas J. Vascular corrosion casting: review of advantages and limitations in the application of some simple quantitative methods. *Microsc Microanal* 2001;7:253–264.